

Strain Driven Anomalous Anisotropic Enhancement in the Thermoelectric Performance of Monolayer MoS₂

Saumen Chaudhuri,¹ Amrita Bhattacharya,² A. K. Das,¹ G. P. Das,³ and B. N. Dev^{4,5,*}

¹*Department of Physics, Indian Institute of Technology Kharagpur, Kharagpur 721302, India*

²*Department of Metallurgical Engineering and Materials Science, IIT Bombay, Mumbai 400076, India*

³*Research Institute for Sustainable Energy, TCG Centres for Research and Education in Science and Technology, Sector V, Salt Lake, Kolkata 700091, India*

⁴*Department of Physics and School of Nano Science and Technology, Indian Institute of Technology Kharagpur, Kharagpur, 721302, India*

⁵*Centre for Quantum Engineering, Research and Education, TCG Centres for Research and Education in Science and Technology, Sector V, Salt Lake, Kolkata 700091, India*
(Dated: August 2, 2023)

First principles density functional theory based calculations have been performed to investigate the strain and temperature induced tunability of the thermoelectric properties of monolayer (ML) MoS₂. Modifications in the electronic and phononic transport properties, under two anisotropic uniaxial strains along the armchair (AC) and zigzag (ZZ) directions, have been explored in detail. Considering the intrinsic carrier-phonon scattering, we found that the charge carrier mobility (μ) and relaxation time (τ) increase remarkably for strains along the ZZ direction. Concomitantly, strain along the ZZ direction significantly reduces the lattice thermal conductivity (κ_L) of ML-MoS₂. The combined effect of shortened phonon relaxation time and group velocity, and the reduced Debye temperature is found to be the driving force behind the lowering of κ_L . The large reduction in κ_L and increase in τ , associated with the strains along the ZZ direction, act in unison to result in enhanced efficiency and hence, improved thermoelectric performance. Nearly 150% enhancement in the thermoelectric efficiency can be achieved with the optimal doping concentration. We, therefore, highlight the significance of in-plane tensile strains, in general, and strains along the ZZ direction, in particular, in improving the thermoelectric performance of ML-MoS₂.

Keywords: DFT, tensile strain, MoS₂, thermoelectric properties

I. INTRODUCTION

Development and large-scale deployment of clean and green energy resources have become a quintessential challenge for mankind [1]. Thermoelectric generators (TEGs), based on the principle of Seebeck effect [2, 3], can convert a temperature difference to useful voltage and thus, are ideally suitable for waste heat recovery [4]. However, the poor efficiency of the TEGs poses the main challenge of thermoelectric research [5]. The thermoelectric device efficiency is primarily dependent on the intrinsic transport properties of constituent thermoelectric materials (TEMs), which is given by the dimensionless quantity ZT, which is also called the figure of merit. $ZT = \frac{S^2 \sigma}{\kappa} T$, where σ is the electrical conductivity, S is the Seebeck coefficient or the thermopower, $\kappa = \kappa_e + \kappa_L$ is the total thermal conductivity, which is the sum of electrical (κ_e) and lattice thermal conductivity (κ_L), at a given temperature T .

To date, the highest ZT values in typical TEMs are reported to be in the range of 2.5 to 3 [6–9] without nanostructuring. Tuning the ZT of a given TEM is an extremely tedious task, since all the electronic transport coefficients viz. the S , σ and κ_e are dependent on the electronic carrier concentration (n) and therefore, can not be tuned individually. However, κ_L is the only quantity which does not directly depend on n . Hence, the two main routes to maximize the ZT are (a) band engineering to maximize the power factor [10, 11] and (b) phonon engineering for lowering the κ_L of the material [12–16].

Due to the low-dimensional structure and the resulting interface phonon scattering and phonon confinement effects, the reduction in κ occurs naturally in 2D materials. With this advantage over their bulk counterparts, various 2D-materials, viz. transition metal dichalcogenides (TMDCs) (e.g., MoS₂, WS₂, MoSe₂, and HfS₂), group IVA-VA compounds (e.g., SnSe, SnS, GeSe) etc., have emerged as potential thermoelectric material with considerably high thermoelectric efficiency [12]. Layered transition metal di-chalcogenides (TMDCs) have drawn tremendous interest due to their stable crystal structure, intrinsic semiconducting nature and high charge carrier mobility [17–21]. Substantial research has been carried out in recent times towards the development of single-layer TMDCs both using simulations

* corresponding author: bhupen.dev@gmail.com

and experiments. Some of the TMDCs such as WS_2 [22], WSe_2 [23], HfS_2 [24], SnSe_2 [25] etc. have shown notably high thermoelectric performance. Apart from that, recently, a novel type of two-dimensional TMDCs, i.e., $(\text{AX})_2$ ($\text{A} = \text{Si, Ge, Sn, Pb}$; $\text{X} = \text{Se, Te}$), has been predicted theoretically to have high thermoelectric efficiency [26]. Besides the single-layer 2D materials, van der Waals (vdW) heterostructures combining various TMDCs have led to an upsurge in research interest due to their superior physical and chemical properties beyond the single parent material [27]. Due to the strong interfacial phonon scattering and the resulting intrinsically low thermal conductivity, the vdW heterostructures offer significantly high thermoelectric performance. Among the various single-layer TMDCs, MoS_2 has been explored extensively as a potential thermoelectric material, both theoretically [28–34] and experimentally [35, 36] and the monolayer (ML) counterpart of MoS_2 appears to be a reasonably good thermoelectric material [28, 31, 33–36]. From experimental investigations, the power factor ($S^2\sigma$) of ML- MoS_2 at room temperature is found to be $8.5 \times 10^{-3} \text{ WK}^{-2}\text{m}^{-1}$, which is the highest among all thermoelectric materials [35]. However, the ZT value obtained for ML- MoS_2 is low and not useful for practical purposes. Infact, a ZT value of only ~ 0.26 at 500 K has been achieved with ML- MoS_2 [34]. Although in some theoretical reports, an improved ZT value is achieved [37], they are well below the values obtained with other TMDCs such as MoSe_2 (0.8), WSe_2 (0.9), WS_2 (1.1), SnSe_2 (2.95), and HfS_2 (1.09) [as shown in [38] and references therein]. The primary reason behind the low thermoelectric efficiency of ML- MoS_2 is its rather high lattice thermal conductivity (κ_L), upon which the ZT value is inversely dependent. The values of κ_L for monolayer MoS_2 at 300 K, found in theory [38] and experiment [39] are 30.1 and $34.5 \text{ Wm}^{-1}\text{K}^{-1}$ respectively. These values of κ_L are considerably higher compared to the κ_L values obtained with other TMDCs at the same temperature, such as WSe_2 ($3.93 \text{ Wm}^{-1}\text{K}^{-1}$) ZrS_2 ($3.29 \text{ Wm}^{-1}\text{K}^{-1}$), ZrSe_2 ($1.2 \text{ Wm}^{-1}\text{K}^{-1}$), HfS_2 ($5.01 \text{ Wm}^{-1}\text{K}^{-1}$), and HfSe_2 ($1.8 \text{ Wm}^{-1}\text{K}^{-1}$) [as shown in [38] and references therein]. The high value of κ_L and the resulting low efficiency hinders the practical application of ML- MoS_2 as a thermoelectric material. Recently, Janus TMDC monolayers, with an X-M-Y ($\text{M} = \text{Mo, W, Hf, Zr}$, and $\text{X/Y} = \text{S, Se, Te}$) sandwich structure have emerged as a plausible solution for future thermoelectric research. The Janus TMDC monolayers possess significantly low lattice thermal conductivity due to their softened phonon dispersion, reduced group velocity and strong phonon anharmonicity [22, 40, 41]. Such features are highly beneficial for thermoelectric applications. For example, owing to the very low lattice thermal conductivity, the Janus WSTe monolayer offers incredibly high thermoelectric efficiency, which is much higher compared to the pure WS_2 monolayer [22].

Efforts have been made to improve the thermoelectric efficiency of ML- MoS_2 . With the application of an external electric field, a significant enhancement in the Seebeck coefficient of ML- MoS_2 has been achieved [42]. Doping with impurity atoms is one of the most studied approaches in improving the thermoelectric performance of a material [14, 43, 44]. However, the introduction of dopants brings a permanent change into the material and sometimes forms a secondary phase as well [14, 43, 44]. Strain engineering, on the other hand, can be a potential alternative to tune the electronic and thermoelectric properties, owing to its simplicity and reversibility [45, 46]. For instance, the thermoelectric performance of monolayer ZrS_2 and HfS_2 is improved via the application of mechanical strain [24, 47]. For monolayer, few-layer and bulk MoS_2 as well, the application of strain has proven to be an efficient way to tune and improve the thermoelectric performance [28]. There have been efforts to implement various in-plane strains on monolayer and few-layer MoS_2 experimentally by growing the films on stretchable polymer [48–53] or lattice-mismatched substrates [54]. Recent reports have demonstrated that very high values of tensile strains for example, 25% on ML-graphene [55] and up to 11% on ML- MoS_2 [56] can be applied using the nano-indentation technique. On the other hand, the application of compressive strain is always associated with the possibility of ripple formation or warping of the film [57, 58]. Thus, from the experimental point of view, the enhancement in the thermoelectric performance is desirable with tensile strains rather than with compressive strains, owing to the convenience of strain application.

ML- MoS_2 is a well-studied thermoelectric material and therefore, its performance has been avidly explored by researchers in the past. However, a wide range of values for the transport parameters prevail in literature for ML- MoS_2 , which makes the understanding of the transport characteristics and the impact of strain on it baffling. Thus, it is essential to explore the transport properties of ML- MoS_2 in greater detail. Earlier it was reported that the thermoelectric efficiency of ML- MoS_2 can be improved by applying in-plane compressive strain [31]. While this is true, the possible improvement that can be achieved with tensile strain is not thoroughly explored, since the impact of strain on the lattice dynamics and phonon transport is not exhaustively studied. Furthermore, certain important aspects, such as the anisotropy in the thermoelectric performance when subjected to in-plane uniaxial tensile strain, or the possible modifications in the charge carrier mobility when stretched along a certain direction (zig-zag or armchair), have not been hitherto reported in the literature. In this work, the electronic and phonon transport properties of ML- MoS_2 and its modification with uniaxial tensile strains along the armchair (AC) and zigzag (ZZ) directions have been explored in detail. The direction-dependent enhancement in the thermoelectric efficiency of single-layer MoS_2 with in-plane strains is highlighted. The underlying mechanism behind the strain-induced anisotropic modifications in the charge carrier transport and phonon dynamics is unveiled through systematic theoretical calculations.

II. COMPUTATIONAL DETAILS

First-principles calculations have been performed using ab-initio density functional theory (DFT) as implemented in the Vienna Ab Initio Simulation Package (VASP) [59, 60] together with projector augmented wave (PAW) potentials to account for the electron-ion interactions [61]. The electronic exchange and correlation (XC) interactions are addressed within the generalized gradient approximation (GGA) of Perdew-Burke-Ernzerhof (PBE) [62]. In order to explore the implication of non-local exchange and correlation on the electronic band structure, hybrid HSE06 functional has been used for some of the relevant cases. A vacuum thickness of 20 Å is used to minimize the interaction between the periodic images of the layers. A well-converged Monkhorst-Pack [63] k-points set of $21 \times 21 \times 1$ together with a plane wave cutoff energy of 450 eV are used for the geometry relaxation, and a well-converged, denser k-mesh is used for the post-relaxation calculations. For all the strained structures, while the scaled lattice parameter is kept fixed, the atomic coordinates are allowed to relax until the forces on the atoms are optimized to be less than 0.01 eV/Å.

To calculate the temperature- and doping-level-dependent changes in the thermoelectric parameters such as the Seebeck coefficient (S), electrical conductivity (σ), power factor ($S^2\sigma$) etc., semi-classical Boltzmann transport theory implemented within the BoltzTraP package [64] is used. The BoltzTraP package calculates the thermoelectric properties under the constant relaxation time approximation (CRTA) and is based on the electronic energy eigenvalues calculated using VASP. To go beyond the CRTA, the charge carrier mobility and relaxation time are calculated explicitly using the AMSET code [65] taking the intrinsic carrier-phonon scattering effects into consideration. The material-specific inputs such as the elastic constants, dielectric constants and the deformation potential are estimated from first-principle calculations using VASP. The absolute deformation potentials [66] of the valence and the conduction bands in all strained cases have been calculated using the vacuum energy level as a reference.

The phonon dispersion curves are calculated based on the supercell approach using the finite displacement method implemented in the phonopy package [67]. The amplitude of the displacements is fixed at 0.015 Å. The second order harmonic interatomic force constants (IFC), required for the phonon dispersion, are calculated using a convergence-checked $4 \times 4 \times 1$ unit cell together with a strict energy convergence criterion of 10^{-8} eV. To investigate the lattice thermal transport, the Boltzmann transport equation (BTE) for phonons is solved under the relaxation time approximation (RTA) as implemented in phono3py [68]. The second- and third-order interatomic force constants (IFC) are calculated using a convergence-checked $4 \times 4 \times 1$ and $2 \times 2 \times 1$ supercell based on the relaxed unit cell, respectively. Fourth- and higher-order IFCs are not taken into consideration due to their presumably small contribution to lattice thermal transport. Well-converged k-meshes are used to sample the Brillouin Zone (BZ) of the supercells. To accurately compute the lattice thermal conductivity both in the unstrained and the strained cases, a dense q-mesh of $51 \times 51 \times 1$ is used to sample the reciprocal spaces of the primitive cells. The mode-resolved lattice thermal conductivity ($\kappa_{L\lambda}$), phonon group velocity (v_λ) and phonon relaxation time (τ_λ) are extracted using python-based extensions as implemented in phonopy-VASP.

Equilibrium molecular dynamics (EMD) calculations have been performed to assess the thermal stability of ML-MoS₂ at different temperatures using the LAMMPS package [69]. The EMD simulations are performed on a sufficiently large supercell of ML-MoS₂ imposing in-plane periodic boundary conditions and using the NPT ensemble [70, 71] within the Stillinger-Weber potential developed by Wen et al. [72]. The system underwent a temperature increase to 300 K, 600 K, 900 K, 1700 K and 2000 K using the Nose-Hoover thermal bath [73] and then equilibrated at a particular temperature for 200 ps to study the thermal stability.

III. RESULTS AND DISCUSSION

A. Unstrained monolayer MoS₂

TABLE I. Calculated lattice parameters of the hexagonal unit cell and the orthorhombic conventional cell of monolayer MoS₂.

Crystal structure	a (Å)	b (Å)	γ (degree)
Hexagonal	3.17	3.17	120
Orthorhombic	3.17	5.51	90

Before going into the details of the strain-induced effects, we first present an overview of the calculated geometrical, electronic and thermoelectric properties of pristine single-layer MoS₂ in the 2H phase. In the hexagonal honeycomb crystal structure of ML-MoS₂, the Mo and S atomic planes are arranged in a “sandwich” type of structure (S - Mo - S) with the Mo and S atoms having trigonal prismatic coordination, as shown in Fig. 1. In order to apply the

mechanical strain along the two non-equivalent lattice directions independently, namely the armchair (AC) and the zigzag (ZZ) directions, an orthorhombic conventional cell (see Fig. 1) containing two Mo atoms and four S atoms has been used instead of the hexagonal unit cell. Thus, in the chosen orthorhombic cell the AC and the ZZ crystallographic directions desirably align with the orthogonal lattice vectors. The optimized lattice parameters of both the cells in the unstrained condition are given in Table I, which are found to be in good agreement with earlier reports [31, 74].

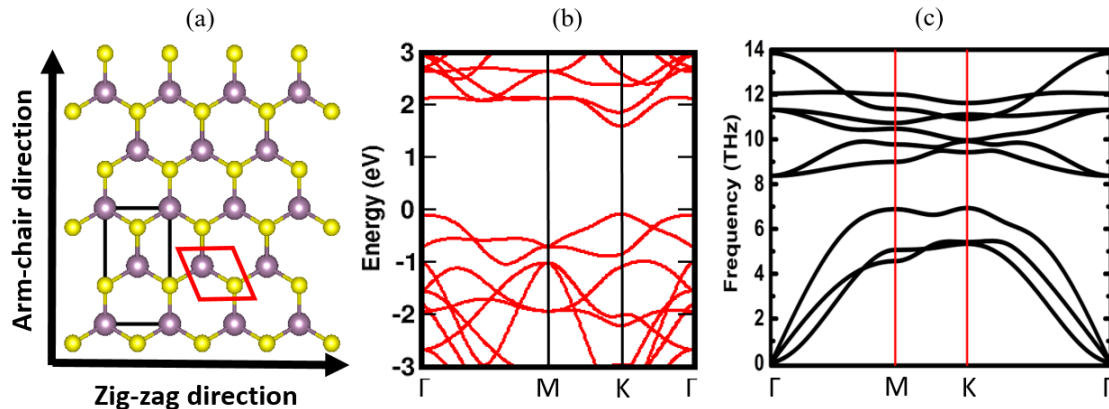


FIG. 1. (a) Crystal structure of monolayer MoS₂ (Mo and S atoms are shown in purple and yellow, respectively). The arrows show the arm-chair and the zig-zag directions. The hexagonal unit cell and the orthorhombic conventional cell are shown by the red and black boxes, respectively. (b) Electronic and (c) phonon band structure of unstrained ML-MoS₂ plotted along the high symmetry path of the irreducible Brillouin zone (BZ).

Unstrained MoS₂ in its monolayer (ML) form is found to be semiconducting with both the valence band maximum (VBM) and the conduction band minimum (CBM) at the same high-symmetry point (at K point) of the BZ, as shown in Fig. 1(b), resulting in a direct band gap semiconductor with a band gap value of 1.736 eV, which agrees well with earlier reports [20, 45, 74]. The band gap value of unstrained ML-MoS₂ from the hybrid functional calculations using the HSE06 functional is found to be 2.184 eV. From Fig. S1 in the supplementary material (see supplementary Sec. A Fig. S1) it can be seen that the electronic band structure of ML-MoS₂ calculated using the GGA-PBE functional and HSE06 functional are nearly identical in terms of the band curvature at the extrema, however the implementation of the hybrid functional increases the band gap by 0.448 eV. Since the electronic band dispersions are well produced using the computationally less expensive GGA-PBE functional, we chose to use the GGA-PBE functional in all further electronic structure calculations. The detailed partial density of states (DOS) and the orbital projected band structure (BS) are provided as supplementary material (see supplementary Sec. A Fig. S2). From the DOS and orbital projected BS, it is seen that both the valence band and conduction band edges are primarily composed of Mo-4*d* and S-3*p* orbitals, albeit mainly Mo-4*d* orbitals [20]. The phonon band structure of unstrained single-layer MoS₂ is also shown in Fig. 1, whereby the absence of imaginary phonon modes throughout the BZ confirms the vibrational stability of the crystal structure. The phonon band structure consists of three low-energy acoustic branches and six optical branches, and they are well separated by a frequency difference of 1.38 THz (46 cm⁻¹). The frequency of the two Raman active modes of ML-MoS₂, namely E_{2g} and A_{1g}, are found to be 11.32 THz (377 cm⁻¹) and 12.04 THz (401 cm⁻¹), respectively. These frequency values are in good agreement with previously reported values [75–77].

The thermoelectric transport parameters of unstrained ML-MoS₂, i.e. the Seebeck coefficient (*S*), relaxation time-scaled electrical conductivity (σ/τ), electronic thermal conductivity (κ_e/τ) and thermoelectric power factor, PF ($S^2\sigma/\tau$) have been calculated with respect to chemical potential (μ) at different temperatures (*T*) and are shown in Fig. 2. The positive ($\mu > 0$) and the negative values ($\mu < 0$) of the chemical potential stand for the n-doping and p-doping regions, respectively. ML-MoS₂ in the unstrained condition exhibits a high *S* of 1590 μVK^{-1} at *T* = 300 K with optimal doping. The variation in the Seebeck coefficient (*S*) as a function of chemical potential (μ) at a particular temperature is found to have saw-tooth nature, which is typical of any semiconducting material. The peak value of the relaxation time-scaled thermoelectric PF at *T* = 300 K is found to be $15.5 \times 10^{10} \text{ Wm}^{-1}\text{K}^{-2}\text{s}^{-1}$ in the n-doping region, which is in good agreement with earlier reports using the same exchange-correlation functional [31, 38]. The variation in the thermoelectric coefficients with temperature has been presented at *T* = 300 K, 600 K and 900 K. With an increase in *T*, the peak value of the *S* and σ/τ decreases. In contrast, the peak value of the PF increases, as shown in Fig. 2, which reaches $36.5 \times 10^{10} \text{ Wm}^{-1}\text{K}^{-2}\text{s}^{-1}$ at *T* = 900 K. This is comparably as high as some of the best-known thermoelectric materials [24, 78]. Over the years various 2D materials have been investigated as a potential thermoelectric material and the maximum attainable power factor (PF_{max}) obtained at room temperature has been reported to be 10×10^{10} , 25×10^{10} and $4 \times 10^{10} \text{ Wm}^{-1}\text{K}^{-2}\text{s}^{-1}$ with WS₂ [78], HfS₂ [24] and PtSe₂ [79], respectively.

Comparing the PF_{\max} alone, ML-MoS₂ stands as a promising thermoelectric material with high potential. In order to calculate the thermoelectric figure of merit ZT , the variation in the κ_L of ML-MoS₂ with temperature has also been investigated. The value of κ_L for ML-MoS₂ nanosheet at 300 K is found to be $24.28 \text{ Wm}^{-1}\text{K}^{-1}$, which is consistent with previously reported theoretical (using MD or DFT framework) [38, 80] and experimental [39] values. Pertaining to the increase in scattering, the κ_L decreases sharply with an increase in temperature and reduces to $7.5 \text{ Wm}^{-1}\text{K}^{-1}$ at 900 K. A similar decreasing trend in κ_L has also been observed in other 2D TMDCs such as WS₂, WSe₂ [81] and HfS₂ [24].

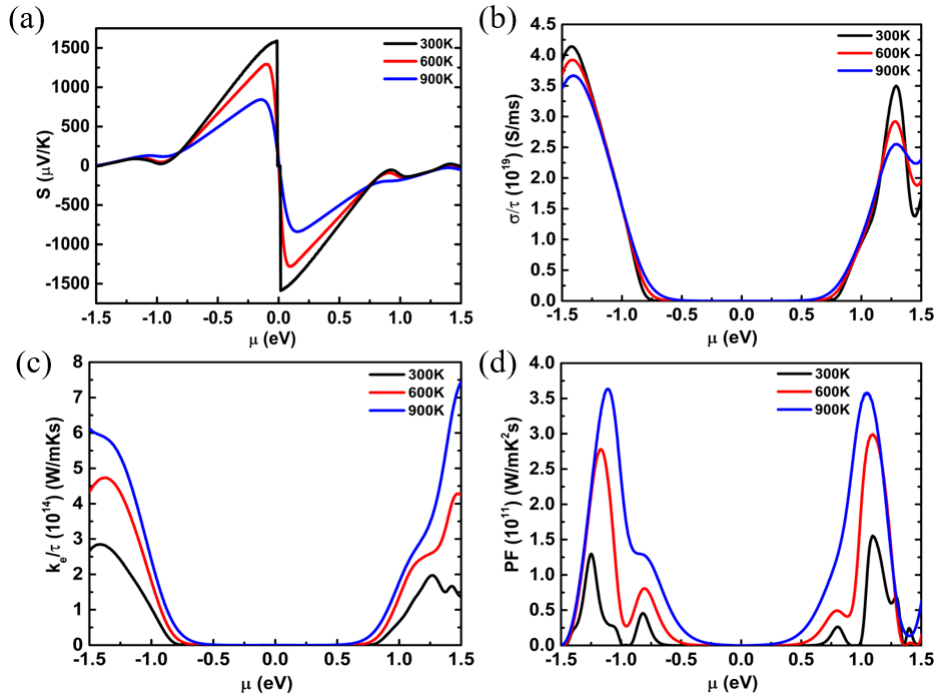


FIG. 2. Variation in the thermoelectric parameters of unstrained ML-MoS₂ viz., (a) Seebeck coefficient (S), (b) electrical conductivity (σ/τ), (c) electronic thermal conductivity (κ_e/τ), and (d) power factor, PF ($S^2\sigma/\tau$) plotted as a function of chemical potential (μ) at different temperatures (i.e. at 300 K, 600 K and 900 K). $\mu > 0$ eV corresponds to the n-type carriers or higher electron concentration, and $\mu < 0$ eV corresponds to the p-type carriers or higher hole concentration.

Since the transport properties of ML-MoS₂ are studied up to a fairly high temperature of 900 K, it is necessary to address the thermal stability of the structure and the possible impact of temperature on the electronic properties. To investigate the thermal stability of ML-MoS₂, molecular dynamics (MD) calculations have been performed at different temperatures up to 2000 K. From the energy plots shown in Fig. S3 (see supplementary Sec. A Fig. S3), it can be seen that the total and the average energy remains stable with obvious temperature induced fluctuations within the simulation time scale for $T = 300$ K, 600 K and 900 K. However, when a high enough temperature is applied, such as say 2000 K, the total energy is found to decrease monotonically with simulation time, indicating the temperature induced instability of the structure. Also, to understand the evolution of the geometry of ML-MoS₂ sheet with the application of temperature, the pair correlation function (PCF) has been calculated as a function of temperature. The PCF represents the probability of finding a pair of atoms at a certain separation distance i.e., the bond length of the constituent atoms (see supplementary Sec. A Fig. S3). Distinct and sharp peaks in the PCF indicate that the perfect crystalline order is maintained up to 900 K and thus, the structure is stable. However, at 1700 K and 2000 K the PCF peaks are diffused and the probability of finding a pair of Mo-S atoms is non-zero at all values of separation distance, which suggests the melting or breakdown of the crystalline order of ML-MoS₂. Thus, it is safe to assume that ML-MoS₂ remains stable at least up to 900 K, which is the highest temperature used in the calculation of transport properties.

To find out an estimate of the effect of temperature on the electronic properties, the linear thermal expansion coefficient (TEC) of ML-MoS₂ is calculated within the quasi-harmonic approximation (qha). Details of the calculation of TEC are provided in the supplementary information and the variation in TEC with temperature is shown in Fig. S4 (see supplementary Sec. A Fig. S4). The TEC of ML-MoS₂ at 300 K and 900 K are found to be 6.3×10^{-6} /K and 7.2×10^{-6} /K, respectively, which are in good agreement with earlier reports [82, 83]. Due to the low values of TEC, it can be assumed that even at the highest temperature considered in the present work (900 K) the lattice expansion

and the resulting impact on the electronic band structure will be insignificant. It is also reported that the thermal shifts in the Raman modes at high temperatures are primarily caused by the multi-phonon scattering and thermal expansion plays a negligibly small role. The reported values of the shift rates (cm^{-1}/K) of the E_{2g} and A_{1g} Raman modes of ML-MoS₂ caused by the thermal expansion are -0.0019 and -0.0010 , respectively [83]. It is, therefore, legitimate to neglect the temperature induced effects on the electronic and phononic band structures of ML-MoS₂.

B. Effect of Strain

1. Effect of strain on electronic properties

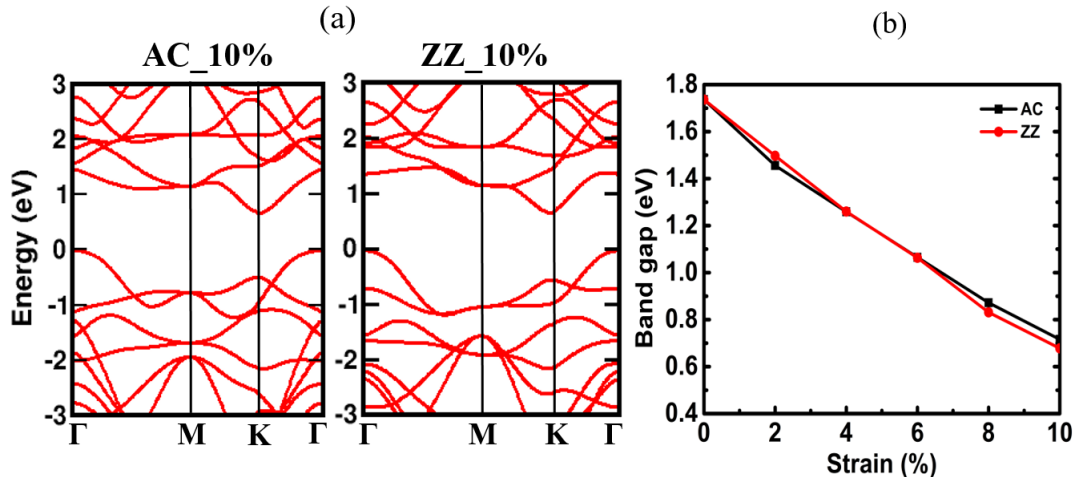


FIG. 3. (a) Band structure plots of ML-MoS₂ in the extreme strained (10%) conditions and (b) variation in the band gap under the uniaxial strain along the AC and the ZZ directions. The strain profile is written at the top of corresponding band structure plots.

To elucidate the importance of strain engineering in tuning the electronic properties of single-layer MoS₂, a series of in-plane uniaxial tensile strains along different directions such as the armchair (AC) and the zigzag (ZZ) direction have been applied. The applied strain is defined as $\epsilon = \frac{a-a_0}{a_0} \times 100\%$, where a_0 and a are the unstrained and strained lattice parameters, respectively. The effect of strain on the band gap and the band structure plots under extreme strain cases (AC_10% and ZZ_10%) using the GGA-PBE functional are shown in Fig. 3, and that using the HSE06 functional are presented in the supplementary material (see supplementary Sec. A Fig. S1). From Fig. S1, it can be seen that not only the band dispersions but also the magnitude of reduction in the band gap under the strained conditions are well captured within the GGA-PBE XC functional. We, therefore, affirm that the choice of the GGA-PBE functional for the electronic structure calculations of ML-MoS₂ is a legitimate one. The band structure plots in the intermediate strain values are shown in Fig. S5 (see supplementary Sec. B Fig. S5). In all strain cases, a direct to indirect band gap transition at low values of strain, followed by a lowering of the band gap is seen. The reduction in the band gap is nearly identical for strains along the AC and the ZZ directions (see Fig. 3 (b)). It can be seen from Fig. 3 (a) that the reduction in the band gap is mainly due to the shifting of the conduction band (CB) edge at K towards the Fermi energy. In the unstrained condition, the valence band edges at K and Γ are nearly degenerate in energy and thereby form two hole-pockets in the valence band edge (see Fig. 1 (b)). With tensile strain, the valence band (VB) edge at K starts to move towards lower energy, shifting the VBM from the K-point to the Γ -point (see Fig. 3). Therefore, only the hole-pocket at Γ remains at the valence band edge in the strained structures. The magnitude of the energy shifts of the VB and the CB edges (i.e. the VBM and CBM) with strain can be seen in Fig. S6 (see supplementary Sec. B Fig. S6). A detailed analysis of how various in-plane strains on ML-MoS₂ can alter the band edge energies has been presented in our previous work [20]. From Fig. S2 in the supplementary material (see supplementary Sec. A Fig. S2) it can be seen that the VB edge at K-point is mainly composed of the in-plane $d_{xy}/d_{x^2-y^2}$ orbitals of Mo, and the VB edge at Γ is composed of the hybridized out-of-plane Mo- d_{z^2} and S- p_z orbitals. The CB edge at the K-point is found to be composed of the Mo- d_{z^2} orbitals in anti-bonding configuration. Strain induced changes in the structural parameters, such as the Mo-S bond length and the S-S interplanar distance, result in changes in the hybridization strength between the Mo-d and S-p orbitals and thereby shifting the VB and the CB edges in energy.

With the application of tensile strain, the Mo-Mo bond length increases, while a decrease is observed in the S-Mo-S bond angle and the S-S interplanar distance. Therefore, under tensile strain, the interaction strength between the out-of-plane Mo- d_{z^2} orbitals is weakened. Thus, with increasing tensile strain, the CB states at K, comprising of the Mo- d_{z^2} orbitals in anti-bonding configuration, shift down in energy.

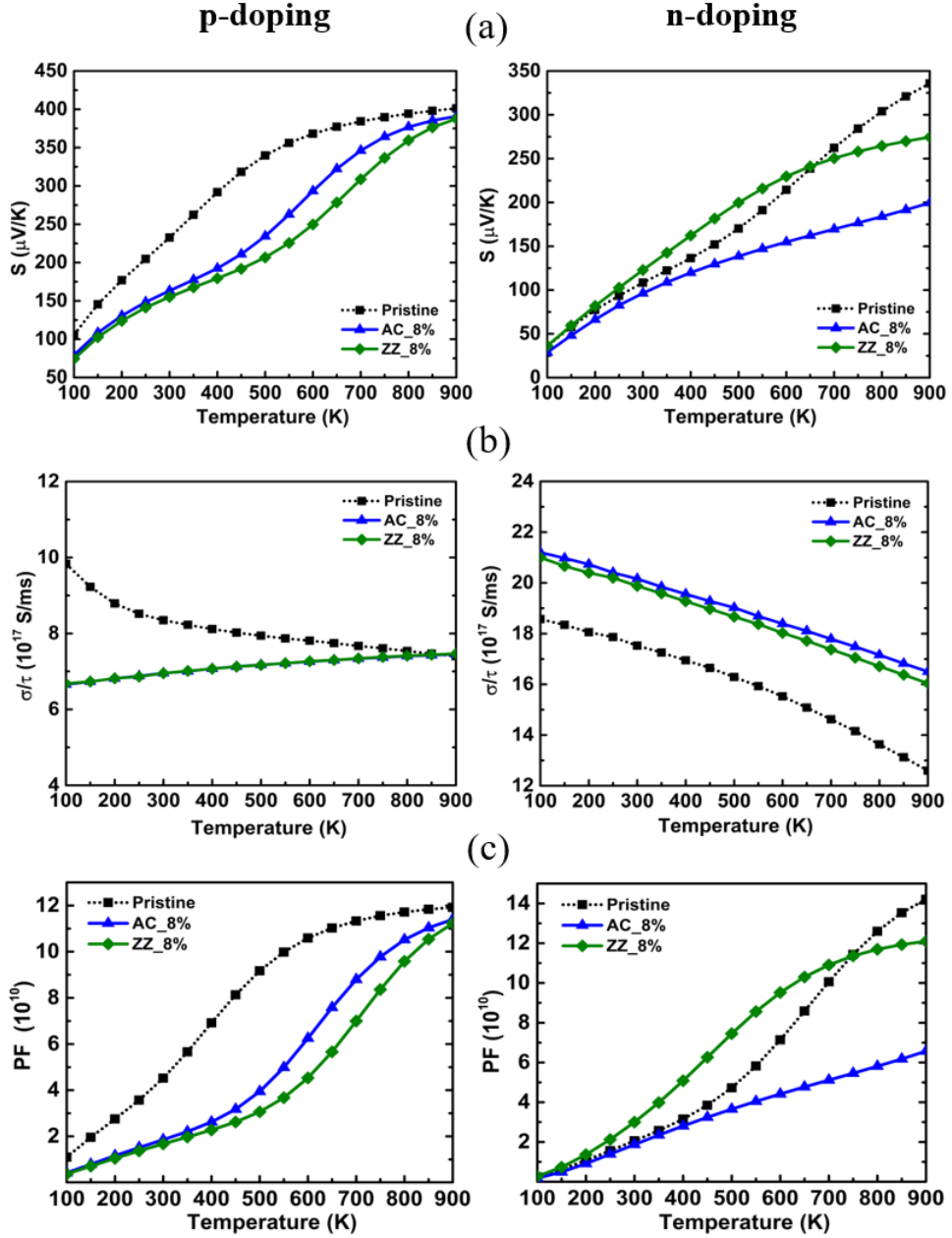


FIG. 4. Variation in the (a) Seebeck coefficient (S), (b) electrical conductivity (σ/τ), and (c) power factor ($S^2\sigma/\tau$) of ML-MoS₂ with temperature at different strain values. The curves for the unstrained structure are shown with the dotted lines. The left panel stands for p-type carriers and the right panel for n-type carriers. The above transport calculations are performed with a fixed doping concentration of $5 \times 10^{19} \text{ cm}^{-3}$ for both p- and n-doping.

2. Effect of strain on thermoelectric properties

The change in electronic structure is expected to influence the transport and thermoelectric properties. The variation in the thermoelectric parameters (S , σ/τ , PF) of single-layer MoS₂ with mechanical strain in a temperature

range of 100 K to 900 K is shown in Fig. 4. In all the thermoelectric calculations, the doping level is kept fixed at $5 \times 10^{19} \text{ cm}^{-3}$ for both p- and n-type carriers. Such a doping concentration has been used in earlier theoretical works [28] and has been achieved also in experiments [35]. Under the action of tensile strains the value of S is found to decrease. Similar observations have also been reported in earlier works [31–33]. For 8% uniaxial strain along the ZZ direction only, the values of S exceed that of the unstrained cases for temperatures up to 700 K, as can be seen from Fig. 4(a). At 300 K, the S value drops from $235 \mu\text{V/K}$ in the unstrained condition to nearly $155 \mu\text{V/K}$ in the strained cases for p-type carriers. The thermopower in the unstrained, as well as the strained cases, is found to increase with temperature for both p and n doping.

From the variation of the relaxation-time-coupled electrical conductivity (σ/τ) with strain and temperature (see Fig. 4(b)), it can be seen that the σ/τ varies differently for p- and n-type carriers under the action of strain. For p-type carriers, the σ/τ decreases with strain, whereas it increases for n-type carriers. Also, the values of σ/τ are higher for n-doping than that of the p-doping for unstrained and strained cases throughout the temperature range 100 K to 900 K. This contrasting behaviour of the p- and n-type carriers can be understood from the dispersion of the valence and conduction band edges of ML-MoS₂. With strain application, the VBM shifts from K-point to Γ -point, where the dispersion is significantly less, whereas the CBM at K-point becomes more dispersive compared to the unstrained condition. The same can be seen from the calculated effective masses associated with the band edges, as discussed later. Due to this highly dispersive nature, the CBM offers very high mobility of the charge carriers. Therefore, the σ/τ of the n-type carriers becomes higher compared to the p-type carriers. The temperature variation of the σ/τ also shows different characteristics for n- and p-type carriers. The changes in σ/τ with temperature remain insignificant for p-type doping, whereas it decreases gradually for n-type doping. This is probably due to the intrinsic n-type nature of monolayer MoS₂ in the pristine condition. With the further addition of n-type carriers, it starts to behave like a degenerate semiconductor and hence, the conductivity falls with increasing temperature. However, to estimate the actual variation in σ with strain and temperature, decoupling of the carrier relaxation time (τ) from σ/τ is necessary.

The usefulness of a thermoelectric material is gauged by its power factor ($S^2\sigma$). The power factor (PF) should be high for a good thermoelectric material. The variation in the relaxation-time-scaled PF ($S^2\sigma/\tau$) of monolayer MoS₂ with strain and temperature is shown in Fig. 4(c). It can be seen that, except for the case of n-doped 8% uniaxial tension along the ZZ direction, the PF value decreases with tensile strain compared to the pristine values throughout the temperature range. In the unstrained condition, owing to the presence of two nearly degenerate hole-pockets in the valence band (at K and Γ), the PF values obtained with p-doping ($\mu < 0$) are higher than that with n-doping ($\mu > 0$). At room temperature, for the unstrained structure, the PF value obtained with p-doping ($4.51 \times 10^{10} \text{ Wm}^{-1}\text{K}^{-2}\text{s}^{-1}$) is twice as high as that with n-doping ($2.05 \times 10^{10} \text{ Wm}^{-1}\text{K}^{-2}\text{s}^{-1}$). With increasing strain, the hole-pocket at K moves downward in energy. Therefore, only the valence band states at Γ , which has much less dispersion, contribute to carrier transport. Owing to the 6-fold degeneracy of the valence band states at K, the density of states effective mass (m_D) is very high in the unstrained condition. However, in the strained cases, the m_D is significantly reduced due to the non-degenerate Γ point. Thus, the power factor falls dramatically with strain for p-type carriers. However, the PF value increases gradually with increasing temperature for both types of carriers. At 900 K, the highest PF value of $14.3 \times 10^{10} \text{ Wm}^{-1}\text{K}^{-2}\text{s}^{-1}$ is obtained with the n-doped unstrained structure, which is higher compared to the values obtained with the strained structures.

It is worth noting that the thermoelectric parameters calculated herein, such as the σ , κ_e , $S^2\sigma$ are scaled by the electronic relaxation time (τ), since all calculations are performed based on the constant relaxation time approximation (CRTA). The CRTA assumes that the electronic relaxation time does not vary strongly with energy. Such an oversimplified assumption, at times, leads to conclusions far from reality. In the present case, the explicit determination of τ is essential, due to the fact that the carrier relaxation time itself is a function of strain. In the calculations of carrier mobility (μ) and relaxation time (τ), the scattering of the charge carriers with phonons i.e., with longitudinal acoustic phonons within the deformation potential theory (ADP) and with polar optical phonons (POP) are considered. Other scattering processes, such as the boundary scattering or ionized impurity scattering may also play a vital role in dictating the actual scattering lifetimes observed in typical experiments. However, they are strongly subjected to experimental parameters and thus, have been ignored henceforth. Due to the non-consideration of these scattering processes, the calculations are expected to provide only an intrinsic limit of the μ and τ , which can be largely overestimated compared to the experimental values. The total mobility of the charge carriers is calculated using the Matthiessen's rule $\mu^{-1} = \sum \mu_i^{-1}$, where i stands for different scattering events, such as ADP and POP. The variation in the total mobility and relaxation time of electrons and holes with strain and temperature are shown in Fig. 5. The individual contribution of the different scattering processes, such as the ADP and POP, towards the total μ and τ , are presented in Fig. S7 and S8 (see supplementary information Sec. B Fig. S7 and S8). It can be seen that the charge carrier transport is mainly governed by the ADP and the contribution from the POP is negligibly small. The inconsequential effect of the POP can be understood due to the intrinsically non-polar nature of MoS₂. Therefore, it is legitimate to focus only on the ADP to understand the effect of strain and temperature on the carrier

transport.

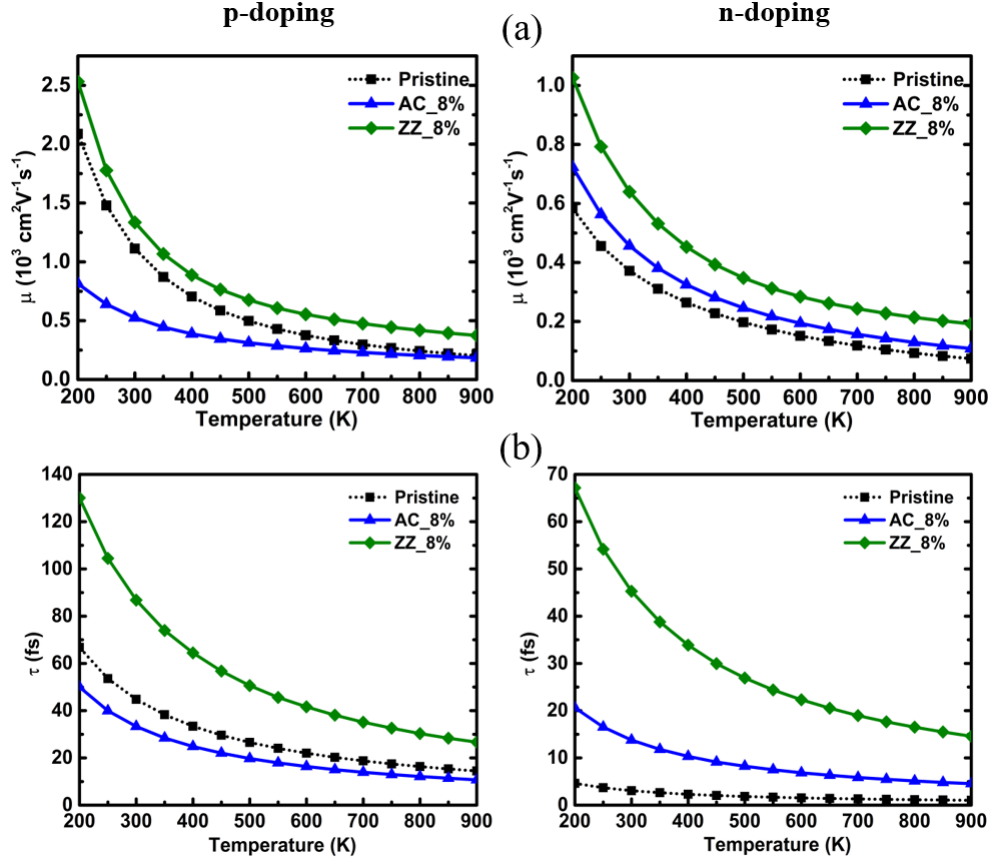


FIG. 5. Variation in the (a) mobility (μ), (b) relaxation time (τ) of the charge carriers of ML-MoS₂ with temperature at different strain values. The curves for the unstrained structure are shown with the dotted lines. The left panel stands for holes and the right panel for electrons.

TABLE II. The calculated physical parameters i.e., the effective mass (m^*) of electrons and holes, the effective 2D elastic constant (C_{2D}) in GPa, and the deformation potential constant (E_{DP}) for the conduction and the valence band edges in eV of ML-MoS₂ in the unstrained and 8% strained cases along the AC and the ZZ directions.

		m^*		C_{2D}		E_{DP}	
		AC	ZZ	AC	ZZ	AC	ZZ
Pristine	e	0.46	0.47	215	215	-6.35	-6.67
	h	0.56	0.59	215	215	-2.54	-2.31
AC_8%	e	0.42	0.40	149	207	-5.43	-5.96
	h	2.5	2.17	149	207	-2.31	-2.01
ZZ_8%	e	0.43	0.39	193	137	-5.38	-5.10
	h	1.32	1.27	193	137	-1.12	-0.98

The variation in the acoustic phonon limited (ADP) carrier transport properties with strain and temperature can be understood using the simplest form of the deformation potential theory of Bardeen and Shockley [84], where the carrier mobility is given as, $\mu = \frac{2e\hbar^3 C_{2D}}{3k_B T m^{*2} (E_{DP})^2}$, where C_{2D} is the effective elastic constant, m^* is the carrier effective mass, and E_{DP} is the deformation potential constant of the VBM for the holes and CBM for the electrons. Note that, the original form of the Bardeen-Shockley equation, as shown here for the sake of simplicity, does not consider the influence of transverse acoustic phonon modes in the calculation of carrier mobility. However, in this work, the effect of transverse phonons and thereby, the anisotropy in the C_{2D} , m^* and E_{DP} have been taken into account in the calculation of deformation potential limited carrier mobility. The calculated elastic constants, effective mass and the deformation potential constants for the unstrained and strained cases are provided in Table II and they are in

good agreement with earlier reports [85–87]. The carrier mobility decreases as a function of temperature following the inverse law, as can be seen from Fig. 5. The mobility of the electrons and holes at 300 K are found to be 368 and 1100 $\text{cm}^2\text{V}^{-1}\text{s}^{-1}$, respectively. Due to the small deformation potential of the VBM, the hole mobilities are found to be much higher compared to the electron mobilities. The room temperature mobilities calculated herein are seemingly higher as compared to the earlier reports [88, 89]. The observed large difference is primarily due to two important factors, one is the consideration of carrier screening in our calculations and the other one is the accurate determination of the absolute deformation potential constant. Since all the electronic transport calculations are done considering a high carrier concentration ($5 \times 10^{19} \text{cm}^{-3}$), it is expected that the large carrier density would impose significant screening and thereby impact the transport properties. Next, the deformation potential constants (E_{DP}) calculated in the earlier studies (10.7, 5.1) are much higher compared to our calculations (6.6, 2.3), due to which the carrier mobilities found therein are much smaller. In the calculation of E_{DP} , it is necessary to compute the changes in the VBM and CBM energies with respect to a fixed reference level. In our calculations, the vacuum energy level is taken as the reference and the values of E_{DP} calculated are found to be in good agreement with the absolute deformation potentials calculated by Pasquarello et al. [85]. To get a comparable estimate with the experimental values, we also calculate the electron mobility of unstrained ML-MoS₂ considering the scattering of the charge carriers with impurity defects in addition to the intrinsic carrier-phonon scattering and presented in Fig. S9 (see supplementary information Sec. B Fig. S9). With the incorporation of the impurity scattering, the μ of electrons at 300 K are found to be 81.1 $\text{cm}^2\text{V}^{-1}\text{s}^{-1}$, which is in good agreement with previous experimental and theoretical investigations [88–90]. Therefore, an overestimated value of μ and τ is obtained when only intrinsic carrier-phonon scattering is taken into consideration. However, we stress that the effect of strain and temperature on the carrier transport, which is the aim of this study, can be well captured within this simplified formulation.

Compared to the carrier mobilities in the unstrained condition, the electron mobilities (μ_e) increase with the application of tensile strain along both the AC and ZZ directions, whereas the hole mobilities increase only for strain along the ZZ direction. With tensile strain, the effective mass of electrons at the CBM (at K point) decreases monotonically with a large decrease in E_{DP} of the conduction band edge, as can be seen from Table II. Therefore, the electron mobility (μ_e) is enhanced with tensile strains at all temperatures from 200 K to 900 K. The magnitude of enhancement in μ_e is higher for strains along the ZZ direction than the AC direction, which can be understood from the larger reductions in m^* and E_{DP} associated with it. The variation in the hole mobility with strain is complex due to the shift of the VBM from the high-disperse K point to the much less-disperse Γ point. The large increase in the hole effective mass (see Table II) resulting from the flat valence band top at Γ governs the hole transport in the strained conditions and thus, results in a large decrease in hole mobility. However, for strains along the ZZ direction, the large reduction in E_{DP} (~ 2.5 times for 8% strain) overshadows the impact of large effective mass and results in higher mobility compared to the pristine cases at all temperatures. The carrier relaxation time (τ) for electrons and holes, shown in Fig. 5, is computed from the sum of the individual scattering rates ($1/\tau$). The strain-induced variation in the individual scattering rates corresponding to ADP and POP are presented in Fig. S8 (see supplementary information Sec. B Fig. S8). The estimated τ values are incorporated in the calculated electronic transport parameters such as the σ/τ , κ_e/τ , $S^2\sigma/\tau$ to get rid of the relaxation time scaling resulting from the CRTA.

Next, the impact of tensile strain on the lattice thermal conductivity (κ_L) is investigated, and the variation in κ_L with strain and temperature is presented in Fig. 6. For unstrained monolayer MoS₂, the value of κ_L at 300 K is found to be 24.28 $\text{Wm}^{-1}\text{K}^{-1}$, which agrees well with earlier reports [38, 39, 80]. With in-plane tensile strains, the value of κ_L decreases throughout the temperature range. However, the rate of decrease strictly depends on the direction of the applied strain. The reduction in κ_L is found to be higher for uniaxial strains along the zigzag (ZZ) direction than along the armchair (AC) direction for all temperatures (see Fig. 6 (d)). The values of κ_L at 300 K for 8% uniaxial strain along the AC and the ZZ direction are found to be 18 $\text{Wm}^{-1}\text{K}^{-1}$ and 14 $\text{Wm}^{-1}\text{K}^{-1}$ respectively, compared to the pristine value of 24.28 $\text{Wm}^{-1}\text{K}^{-1}$. Such anisotropic reduction in κ_L with strain can be understood from the difference in atomic coordination along the two non-equivalent directions, where unique nearest neighbour (NN) patterns can be seen. Each S atom at the edge possesses two NN Mo atoms, each of which has three NN S atoms along the ZZ direction, while along the AC direction, one Mo atom has two and the other one has three NN S atoms. Due to this difference in nearest neighbour counting, the applied strain of equal magnitude has a different impact on κ_L along the two directions (AC and ZZ). Also, the κ_L values decrease gradually with increasing temperature following the $\frac{1}{T}$ law owing to the increased probability of Umklapp scattering and becoming less than 5 $\text{Wm}^{-1}\text{K}^{-1}$ at 900 K for strains applied along the ZZ direction. The total thermal conductivity computed by adding the electronic (κ_e) and the lattice contribution (κ_L), is provided in Fig. S10 (see supplementary Sec. C Fig. S10). At all strain values and temperatures, the total thermal conductivity is dominated by the lattice counterpart. The electronic contribution is at least two orders of magnitude lower than the lattice contribution, as shown in Fig. S10 (see supplementary Sec. C Fig. S10). This can be understood as the calculations are done within the semiconductor regime of ML-MoS₂, and for a semiconductor, the majority of the heat is carried by the phonons with negligible contribution stemming from

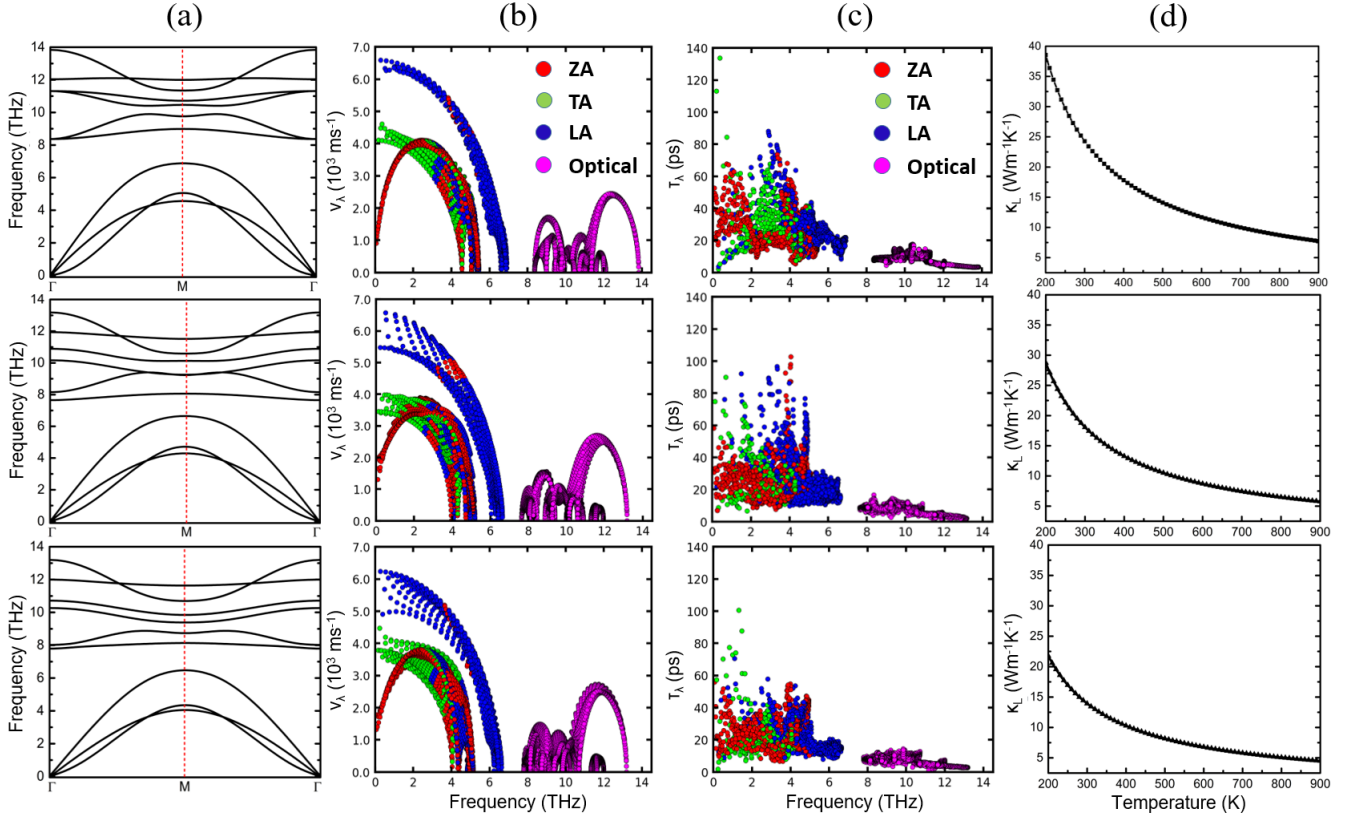


FIG. 6. (a) Phonon band structures plotted along the high symmetry path, (b) phonon group velocity (v_λ) plotted as a function of frequency (c) relaxation time (τ_λ) plotted as a function of frequency at 300 K, and (d) lattice thermal conductivity (κ_L) plotted as a function of temperature for the unstrained (top panel), 8% uniaxially strained structures along the armchair (middle panel) and the zigzag (bottom panel) direction.

the electrons.

To investigate the strain-induced large and anisotropic reduction in κ_L in greater detail, further analysis of the κ_L at 300 K is performed. From the cumulative lattice thermal conductivity (κ_{Lc}) (see supplementary Sec. C Fig. S11), it is clear that almost the entire contribution towards κ_L is coming from the frequencies below 7 THz i.e., from the acoustic phonon modes, as expected. The contribution coming from the optical modes is negligible. To investigate the contribution from individual acoustic modes, modal-decomposed values of κ_L and various other parameters that help in the analytical modelling of κ_L such as the specific heat (C_λ), group velocity (v_λ) and relaxation time (τ_λ) of a particular phonon mode λ are computed at 300 K and are presented with the phonon band structures in Fig. 6. From the mode resolved κ_L shown in Fig. S12 (see supplementary Sec. C Fig. S12), it is clear that the contribution stemming from the three acoustic modes is reduced under the action of tensile strains. Both the v_λ and τ_λ of the acoustic modes are considerably higher compared to the optical modes and thus, the acoustic modes dominate the heat transport mechanism. With increasing strain, both v_λ and τ_λ decrease, although the reduction in τ_λ is found to be more pronounced. Also, the reduction in τ_λ for strains along the ZZ direction is higher than that for the AC direction. Due to the reduction in τ_λ , the phonon mean free path reduces and the phonon scattering probability increases significantly. As a result, the κ_L decreases with strain and a larger degree of reduction occurs for strain along the ZZ direction. In MoS₂, as well as other 2D-TMDCs, the ZA mode is seen to be the dominant heat conduction carrier and the frequency gap between the ZA and the optical modes determines the intensity of the phonon scattering [24, 91]. The smaller the frequency gap, the stronger the scattering and the lower the κ_L . In an earlier report [20], it has been observed that with in-plane tensile strains, the ZA-optical frequency gap of ML-MoS₂ decreases. This reduction in frequency gap may result in an enhanced ZA-optical phonon scattering and thereby, the κ_L of ML-MoS₂ is further lowered under the action of tensile strains.

Furthermore, the high κ_L of pristine ML-MoS₂ results from the low average atomic mass and the strong in-plane covalent bonding between the Mo and the S atoms. Strong interatomic bonding and low average atomic mass results in larger Debye temperature (θ_D) and higher sound velocity, which in turn results in higher lattice thermal conductivity.

TABLE III. Phonon parameters of single-layer MoS₂ in the unstrained and 8% strained conditions along the AC (AC_8%) and the ZZ (ZZ_8%) directions for the three acoustic modes (labelled according to polarization): group velocity (v_λ) at Γ point in 10^3 ms^{-1} and acoustic Debye temperature (θ_D) in K.

Strain profile	v_{λ_ZA}	v_{λ_TA}	v_{λ_LA}	θ_{D_ZA}	θ_{D_TA}	θ_{D_LA}
Unstrained	0.81	4.38	6.46	246	223	334
AC_8%	1.27	3.61	5.7	230	209	322
ZZ_8%	1.27	3.75	6.15	212	197	314

The modal group velocity (v_λ) near the zone centre (Γ) and the Debye temperature (θ_D) at the zone boundary of the acoustic phonon modes are listed in Table III, which are in good agreement with previous reports [92]. It can be seen that both the v_λ and the θ_D decrease with the application of strain and thus, result in the lowering of the κ_L according to Slack's expression [93]. With tensile strain, the orbital overlap of the Mo and S atoms decreases and therefore, the interatomic bond becomes weaker. Thus, the Debye temperature decreases with increasing tensile strain. The reduction in θ_D is higher when the strain is applied along the zigzag direction (see Table II) and thereby results in a greater reduction of κ_L compared to that of the armchair direction. The strain-induced changes in the acoustic v_λ are not significant and are mostly shadowed by the large changes in the τ_λ . Also, the anharmonicity or the Grüneisen parameter of a material controls the ability of heat transportation through the crystal lattice. The modal Grüneisen parameter of ML-MoS₂ is calculated in order to understand the degree of anharmonicity of the material. No significant change in the Grüneisen parameter is observed in the strained cases compared to the unstrained values (see supplementary sec. C Fig. S13). Thus, the strain-induced anisotropic reduction in κ_L is primarily due to the anisotropic changes in the bond parameters and the resulting θ_D of the acoustic phonon modes.

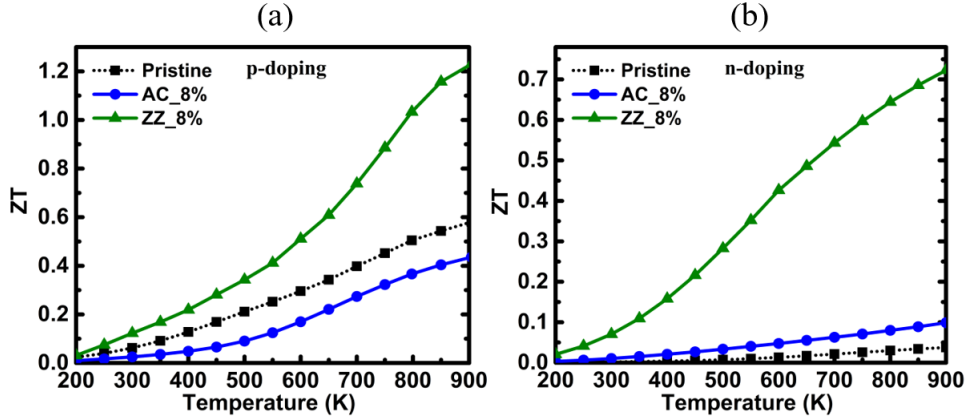


FIG. 7. The variation in thermoelectric figure of merit ZT of ML-MoS₂ with temperature at different tensile strains for (a) p-doping and (b) n-doping.

Finally, combining all the calculated transport parameters (S , σ , τ , κ), the thermoelectric efficiency of ML-MoS₂ is estimated and its variation with chemical potential (μ) and temperature (T) in the unstrained condition is explored (see supplementary Sec. C Fig. S14). The results show that the maximum value of ZT for pristine MoS₂ at 300 K for both p-type and n-type doping is less than 0.1. Such a low value of ZT is not useful for practical applications. However, the ZT value is found to increase sharply with temperature and reach close to 0.7 at 900 K for p-type carriers, suggesting that ML-MoS₂ can be an ideal candidate for high temperature thermoelectric applications.

The impact of strain and temperature on the ZT of ML-MoS₂ at a fixed doping concentration of $5 \times 10^{19} \text{ cm}^{-3}$ is investigated and the results are displayed in Fig. 7(a) and (b). For both p- and n-doping, the ZT values of the strained cases exceed that of the unstrained values throughout the temperature range and higher ZT values can be obtained when the strain is applied along the ZZ direction. The peak ZT values obtained at 900 K for p- and n-doping with 8% uniaxial strain along the ZZ direction are 1.22 and 0.72, respectively. These ZT values are significantly higher compared to the peak values obtained with the unstrained structure (0.58 and 0.03) and the 8% strained structure along the AC direction (0.43 and 0.09). The larger enhancement in charge carrier relaxation time and greater reduction in κ_L for strains along the ZZ direction act in unison to result in the higher ZT values compared to that for strains along the AC direction. From the larger values of ZT for holes and its variation with strain, it is clear that the charge carrier relaxation time (τ) has significant control on the overall thermoelectric performance of ML-MoS₂. Therefore, it is wise to go beyond CRTA, and the explicit determination of τ is necessary. It is worth noting that the enhanced

thermoelectric performance is not only achieved at the specific doping concentration of $5 \times 10^{19} \text{ cm}^{-3}$ or a high strain value of 8%; instead, the enhancement can be achieved for a range of doping concentrations and even with lower strain values. To further support this point, the variation in ZT at 900 K as a function of chemical potential under 4% and 8% uniaxial tensile strains along the AC and ZZ directions are calculated and shown in Fig. S15 (see supplementary Sec. C Fig. S15). It is clear that a much-improved thermoelectric performance can be achieved with the strained structures at the optimal doping concentration. The degree of enhancement, though, strictly depends on the direction and magnitude of the strain applied. The ZT values obtained with the strained cases exceed that of the unstrained case throughout the range of chemical potential or the corresponding doping concentrations. A peak ZT value of 1.7 can be achieved with the hole-doped ML-MoS₂ under 8% uniaxial strain along the zigzag direction. Compared to the peak ZT value of 0.7 obtained with the hole-doped unstrained structure, an enhancement of nearly 150% is possible with the strained structures.

IV. CONCLUSIONS

In summary, the anisotropic tuning of the transport and thermoelectric properties of monolayer MoS₂ with the application of in-plane tensile strains along the armchair (AC) and the zigzag (ZZ) direction has been explored based on first-principles calculations. Both the electronic and phononic transport properties of single-layer MoS₂ change anisotropically with the application of direction-dependent mechanical strains, suggesting that strain engineering can be an efficient way to tune the thermoelectric properties of ML-MoS₂. The Seebeck coefficient (S) and the power factor ($S^2\sigma/\tau$) of ML-MoS₂ decrease with tensile strains for both p- and n-type carriers. However, the reduction is more pronounced for p-type carriers. This is understood from the strain-induced reduction in the number of degenerate hole-pockets in the valence band edge. Although the power factor decreases, the thermoelectric efficiency of ML-MoS₂ is found to increase due to the large reduction in lattice thermal conductivity (κ_L) and the significant increase in charge carrier relaxation time (τ) with tensile strain. Notably, the reduction in κ_L and increase in τ associated with the tensile strains along the ZZ direction are significantly higher compared to the strains along the AC direction. Therefore, a large enhancement in ZT is achieved with the structures strained along the ZZ direction. With optimal doping at 900 K, a ZT value as high as 1.7 is achieved with the strained structures compared to the peak ZT value of 0.7 in the unstrained structure and structures strained along the AC direction. This study, therefore, highlights the importance of direction-specific tensile strains in improving the overall transport characteristics of ML-MoS₂. The proposed mechanism to enhance thermoelectric performance is expected to be equally useful for all other semiconducting TMDCs with an analogous crystal structure.

ACKNOWLEDGMENTS

The first-principles calculations are performed using the supercomputing facility of IIT Kharagpur established under the National Supercomputing Mission (NSM), Government of India and supported by the Centre for Development of Advanced Computing (CDAC), Pune. AB acknowledges SERB POWER grant (SPG/2021/003874) and BRNS regular grant (BRNS/37098) for the financial assistance. SC acknowledges MHRD, India, for financial support.

-
- [1] Owusu, P. A.; Asumadu-Sarkodie, S. A review of renewable energy sources, sustainability issues and climate change mitigation. *Cogent Engineering* **2016**, *3*, 1167990.
 - [2] Zhang, X.; Zhao, L.-D. Thermoelectric materials: Energy conversion between heat and electricity. *Journal of Materiomics* **2015**, *1*, 92–105.
 - [3] Freer, R.; Powell, A. V. Realising the potential of thermoelectric technology: A Roadmap. *Journal of Materials Chemistry C* **2020**, *8*, 441–463.
 - [4] Orr, B.; Akbarzadeh, A. Prospects of waste heat recovery and power generation using thermoelectric generators. *Energy Procedia* **2017**, *110*, 250–255.
 - [5] Liu, W.; Jie, Q.; Kim, H. S.; Ren, Z. Current progress and future challenges in thermoelectric power generation: From materials to devices. *Acta Materialia* **2015**, *87*, 357–376.
 - [6] Patel, A.; Singh, D.; Sonvane, Y.; Thakor, P.; Ahuja, R. Bulk and monolayer As₂S₃ as promising thermoelectric material with high conversion performance. *Computational materials science* **2020**, *183*, 109913.
 - [7] Beretta, D.; Neophytou, N.; Hodges, J. M.; Kanatzidis, M. G.; Narducci, D.; Martin-Gonzalez, M.; Beekman, M.; Balke, B.; Cerretti, G.; Tremel, W., et al. Thermoelectrics: From history, a window to the future. *Materials Science and Engineering: R: Reports* **2019**, *138*, 100501.

- [8] Zhao, L.-D.; Lo, S.-H.; Zhang, Y.; Sun, H.; Tan, G.; Uher, C.; Wolverton, C.; Dravid, V. P.; Kanatzidis, M. G. Ultralow thermal conductivity and high thermoelectric figure of merit in SnSe crystals. *Nature* **2014**, *508*, 373–377.
- [9] Nshimiyimana, E.; Hao, S.; Su, X.; Zhang, C.; Liu, W.; Yan, Y.; Uher, C.; Wolverton, C.; Kanatzidis, M. G.; Tang, X. Discordant nature of Cd in GeTe enhances phonon scattering and improves band convergence for high thermoelectric performance. *Journal of Materials Chemistry A* **2020**, *8*, 1193–1204.
- [10] Bilc, D. I.; Hautier, G.; Waroquiers, D.; Rignanese, G.-M.; Ghosez, P. Low-dimensional transport and large thermoelectric power factors in bulk semiconductors by band engineering of highly directional electronic states. *Physical review letters* **2015**, *114*, 136601.
- [11] Pei, Y.; Shi, X.; LaLonde, A.; Wang, H.; Chen, L.; Snyder, G. J. Convergence of electronic bands for high performance bulk thermoelectrics. *Nature* **2011**, *473*, 66–69.
- [12] Dresselhaus, M. S.; Chen, G.; Tang, M. Y.; Yang, R.; Lee, H.; Wang, D.; Ren, Z.; Fleurial, J.-P.; Gogna, P. New directions for low-dimensional thermoelectric materials. *Advanced materials* **2007**, *19*, 1043–1053.
- [13] Zhang, P.; Gong, L.; Lou, Z.; Xu, J.; Cao, S.; Zhu, J.; Yan, H.; Gao, F. Reduced lattice thermal conductivity of perovskite-type high-entropy (Ca_{0.25}Sr_{0.25}Ba_{0.25}RE_{0.25})TiO₃ ceramics by phonon engineering for thermoelectric applications. *Journal of Alloys and Compounds* **2022**, *898*, 162858.
- [14] Gautam, A. K.; Faraz, M.; Khare, N. Enhanced thermoelectric properties of MoS₂ with the incorporation of reduced graphene oxide (RGO). *Journal of Alloys and Compounds* **2020**, *838*, 155673.
- [15] Li, H.-p.; Zhang, R.-q. Vacancy-defect-induced diminution of thermal conductivity in silicene. *EPL (Europhysics Letters)* **2012**, *99*, 36001.
- [16] Ding, Z.; Pei, Q.-X.; Jiang, J.-W.; Zhang, Y.-W. Manipulating the thermal conductivity of monolayer MoS₂ via lattice defect and strain engineering. *The Journal of Physical Chemistry C* **2015**, *119*, 16358–16365.
- [17] Wang, Q. H.; Kalantar-Zadeh, K.; Kis, A.; Coleman, J. N.; Strano, M. S. Electronics and optoelectronics of two-dimensional transition metal dichalcogenides. *Nature nanotechnology* **2012**, *7*, 699–712.
- [18] Guo, H.-H.; Yang, T.; Tao, P.; Zhang, Z.-D. Theoretical study of thermoelectric properties of MoS₂. *Chinese Physics B* **2013**, *23*, 017201.
- [19] Akinwande, D.; Petrone, N.; Hone, J. Two-dimensional flexible nanoelectronics. *Nature communications* **2014**, *5*, 1–12.
- [20] Chaudhuri, S.; Das, A.; Das, G.; Dev, B. Strain induced effects on the electronic and phononic properties of 2H and 1T' monolayer MoS₂. *arXiv preprint arXiv:2201.02174* **2022**,
- [21] Radisavljevic, B.; Radenovic, A.; Brivio, J.; Giacometti, V.; Kis, A. Single-layer MoS₂ transistors. *Nature nanotechnology* **2011**, *6*, 147–150.
- [22] Patel, A.; Singh, D.; Sonvane, Y.; Thakor, P.; Ahuja, R. High thermoelectric performance in two-dimensional Janus monolayer material WS-X (X= Se and Te). *ACS applied materials & interfaces* **2020**, *12*, 46212–46219.
- [23] Kumar, S.; Schwingenschlogl, U. Thermoelectric response of bulk and monolayer MoSe₂ and WSe₂. *Chemistry of Materials* **2015**, *27*, 1278–1284.
- [24] Wang, H.; Lan, Y.-S.; Dai, B.; Zhang, X.-W.; Wang, Z.-G.; Ge, N.-N. Improved Thermoelectric Performance of Monolayer HfS₂ by Strain Engineering. *ACS omega* **2021**, *6*, 29820–29829.
- [25] Su, Y.; Ebrish, M. A.; Olson, E. J.; Koester, S. J. SnSe₂ field-effect transistors with high drive current. *Applied Physics Letters* **2013**, *103*, 263104.
- [26] Jia, P.-Z.; Xie, Z.-X.; Deng, Y.-X.; Zhang, Y.; Tang, L.-M.; Zhou, W.-X.; Chen, K.-Q. High thermoelectric performance induced by strong anharmonic effects in monolayer (PbX)₂ (X= S, Se, Te). *Applied Physics Letters* **2022**, *121*, 043901.
- [27] Jia, P.-Z.; Xie, J.-P.; Chen, X.-K.; Zhang, Y.; Yu, X.; Zeng, Y.-J.; Xie, Z.; Deng, Y.-X.; Zhou, W.-X. Recent progress of two-dimensional heterostructures for thermoelectric applications. *Journal of Physics: Condensed Matter* **2022**,
- [28] Bhattacharyya, S.; Pandey, T.; Singh, A. K. Effect of strain on electronic and thermoelectric properties of few layers to bulk MoS₂. *Nanotechnology* **2014**, *25*, 465701.
- [29] Huang, W.; Luo, X.; Gan, C. K.; Quek, S. Y.; Liang, G. Theoretical study of thermoelectric properties of few-layer MoS₂ and WSe₂. *Physical Chemistry Chemical Physics* **2014**, *16*, 10866–10874.
- [30] Wickramaratne, D.; Zahid, F.; Lake, R. K. Electronic and thermoelectric properties of few-layer transition metal dichalcogenides. *The Journal of chemical physics* **2014**, *140*, 124710.
- [31] Jena, N.; De Sarkar, A., et al. Compressive strain induced enhancement in thermoelectric-power-factor in monolayer MoS₂ nanosheet. *Journal of Physics: Condensed Matter* **2017**, *29*, 225501.
- [32] Guo, H.; Yang, T.; Tao, P.; Wang, Y.; Zhang, Z. High pressure effect on structure, electronic structure, and thermoelectric properties of MoS₂. *Journal of Applied Physics* **2013**, *113*, 013709.
- [33] Xiang, J.; Ali, R. N.; Yang, Y.; Zheng, Z.; Xiang, B.; Cui, X. Monolayer MoS₂ thermoelectric properties engineering via strain effect. *Physica E: Low-dimensional Systems and Nanostructures* **2019**, *109*, 248–252.
- [34] Jin, Z.; Liao, Q.; Fang, H.; Liu, Z.; Liu, W.; Ding, Z.; Luo, T.; Yang, N. A revisit to high thermoelectric performance of single-layer MoS₂. *Scientific reports* **2015**, *5*, 1–7.
- [35] Hippalgaonkar, K.; Wang, Y.; Ye, Y.; Qiu, D. Y.; Zhu, H.; Wang, Y.; Moore, J.; Louie, S. G.; Zhang, X. High thermoelectric power factor in two-dimensional crystals of Mo S₂. *Physical Review B* **2017**, *95*, 115407.
- [36] Kayyalha, M.; Maassen, J.; Lundstrom, M.; Shi, L.; Chen, Y. P. Gate-tunable and thickness-dependent electronic and thermoelectric transport in few-layer MoS₂. *Journal of Applied Physics* **2016**, *120*, 134305.
- [37] Huang, W.; Da, H.; Liang, G. Thermoelectric performance of mx₂ (m= mo, w; x= s, se) monolayers. *Journal of Applied Physics* **2013**, *113*, 104304.
- [38] Rai, D.; Vu, T. V.; Laref, A.; Hossain, M. A.; Haque, E.; Ahmad, S.; Khenata, R.; Thapa, R. Electronic properties and low lattice thermal conductivity (κ l) of mono-layer (ML) MoS₂: FP-LAPW incorporated with spin-orbit coupling (SOC).

Rsc Advances **2020**, *10*, 18830–18840.

- [39] Yan, R.; Simpson, J. R.; Bertolazzi, S.; Brivio, J.; Watson, M.; Wu, X.; Kis, A.; Luo, T.; Hight Walker, A. R.; Xing, H. G. Thermal conductivity of monolayer molybdenum disulfide obtained from temperature-dependent Raman spectroscopy. *ACS nano* **2014**, *8*, 986–993.
- [40] Bera, J.; Betal, A.; Sahu, S. Ultralow lattice thermal conductivity and high thermoelectric performance near room temperature of Janus monolayer HfSSe. *arXiv preprint arXiv:2003.02439* **2020**,
- [41] Guo, S.-D. Phonon transport in Janus monolayer MoSSe: a first-principles study. *Physical Chemistry Chemical Physics* **2018**, *20*, 7236–7242.
- [42] Buscema, M.; Barkelid, M.; Zwiller, V.; van der Zant, H. S.; Steele, G. A.; Castellanos-Gomez, A. Large and tunable photothermoelectric effect in single-layer MoS₂. *Nano letters* **2013**, *13*, 358–363.
- [43] Kong, S.; Wu, T.; Zhuang, W.; Jiang, P.; Bao, X. Realizing p-type MoS₂ with enhanced thermoelectric performance by embedding VMo₂S₄ nano-inclusions. *The Journal of Physical Chemistry B* **2018**, *122*, 713–720.
- [44] Gangwar, P.; Kumar, S.; Khare, N. Ultrahigh thermoelectric performance of 2H-MoS₂ nanosheets with incorporated conducting secondary phase. *Materials Research Express* **2019**, *6*, 105062.
- [45] Das, R.; Rakshit, B.; Debnath, S.; Mahadevan, P. Microscopic model for the strain-driven direct to indirect band-gap transition in monolayer MoS₂ and ZnO. *Physical Review B* **2014**, *89*, 115201.
- [46] Guzman, D. M.; Strachan, A. Role of strain on electronic and mechanical response of semiconducting transition-metal dichalcogenide monolayers: An ab-initio study. *Journal of Applied Physics* **2014**, *115*, 243701.
- [47] Lv, H.; Lu, W.; Shao, D.; Lu, H.; Sun, Y. Strain-induced enhancement in the thermoelectric performance of a ZrS₂ monolayer. *Journal of Materials Chemistry C* **2016**, *4*, 4538–4545.
- [48] Pu, J.; Zhang, Y.; Wada, Y.; Tse-Wei Wang, J.; Li, L.-J.; Iwasa, Y.; Takenobu, T. Fabrication of stretchable MoS₂ thin-film transistors using elastic ion-gel gate dielectrics. *Applied Physics Letters* **2013**, *103*, 023505.
- [49] Rice, C.; Young, R.; Zan, R.; Bangert, U.; Wolverson, D.; Georgiou, T.; Jalil, R.; Novoselov, K. Raman-scattering measurements and first-principles calculations of strain-induced phonon shifts in monolayer MoS₂. *Physical Review B* **2013**, *87*, 081307.
- [50] Castellanos-Gomez, A.; Roldán, R.; Cappelluti, E.; Buscema, M.; Guinea, F.; van der Zant, H. S.; Steele, G. A. Local strain engineering in atomically thin MoS₂. *Nano letters* **2013**, *13*, 5361–5366.
- [51] Zhu, C.; Wang, G.; Liu, B.; Marie, X.; Qiao, X.; Zhang, X.; Wu, X.; Fan, H.; Tan, P.; Amand, T., et al. Strain tuning of optical emission energy and polarization in monolayer and bilayer MoS₂. *Physical Review B* **2013**, *88*, 121301.
- [52] Conley, H. J.; Wang, B.; Ziegler, J. I.; Haglund Jr, R. F.; Pantelides, S. T.; Bolotin, K. I. Bandgap engineering of strained monolayer and bilayer MoS₂. *Nano letters* **2013**, *13*, 3626–3630.
- [53] Tan, C.; Wong, W.; Ng, S.; Wong, H.; Leung, C.; Mak, C. Raman studies of MoS₂ under strain at different uniaxial directions. *Vacuum* **2018**, *153*, 274–276.
- [54] Ji, Q.; Zhang, Y.; Gao, T.; Zhang, Y.; Ma, D.; Liu, M.; Chen, Y.; Qiao, X.; Tan, P.-H.; Kan, M., et al. Epitaxial monolayer MoS₂ on mica with novel photoluminescence. *Nano letters* **2013**, *13*, 3870–3877.
- [55] Lee, C.; Wei, X.; Kysar, J. W.; Hone, J. Measurement of the elastic properties and intrinsic strength of monolayer graphene. *science* **2008**, *321*, 385–388.
- [56] Bertolazzi, S.; Brivio, J.; Kis, A. Stretching and breaking of ultrathin MoS₂. *ACS nano* **2011**, *5*, 9703–9709.
- [57] Jiang, J. W. The buckling of single-layer MoS₂ under uniaxial compression. *Nanotechnology* **2014**, *25*, 355402.
- [58] Li, Y.; Chen, P.; Zhang, C.; Peng, J.; Gao, F.; Liu, H. Molecular dynamics simulation on the buckling of single-layer MoS₂ sheet with defects under uniaxial compression. *Computational Materials Science* **2019**, *162*, 116–123.
- [59] Kresse, G.; Furthmüller, J. Efficient iterative schemes for ab initio total-energy calculations using a plane-wave basis set. *Physical review B* **1996**, *54*, 11169.
- [60] Kresse, G.; Furthmüller, J. Efficiency of ab-initio total energy calculations for metals and semiconductors using a plane-wave basis set. *Computational materials science* **1996**, *6*, 15–50.
- [61] Kresse, G.; Joubert, D. From ultrasoft pseudopotentials to the projector augmented-wave method. *Physical review b* **1999**, *59*, 1758.
- [62] Perdew, J. P.; Burke, K.; Ernzerhof, M. Generalized gradient approximation made simple. *Physical review letters* **1996**, *77*, 3865.
- [63] Monkhorst, H. J.; Pack, J. D. Special points for Brillouin-zone integrations. *Physical review B* **1976**, *13*, 5188.
- [64] Madsen, G. K.; Singh, D. J. BoltzTraP. A code for calculating band-structure dependent quantities. *Computer Physics Communications* **2006**, *175*, 67–71.
- [65] Ganose, A. M.; Park, J.; Faghaninia, A.; Woods-Robinson, R.; Persson, K. A.; Jain, A. Efficient calculation of carrier scattering rates from first principles. *Nature communications* **2021**, *12*, 1–9.
- [66] Resta, R.; Colombo, L.; Baroni, S. Absolute deformation potentials in semiconductors. *Physical Review B* **1990**, *41*, 12358.
- [67] Togo, A.; Tanaka, I. First principles phonon calculations in materials science. *Scripta Materialia* **2015**, *108*, 1–5.
- [68] Togo, A.; Chaput, L.; Tanaka, I. Distributions of phonon lifetimes in Brillouin zones. *Physical Review B* **2015**, *91*, 094306.
- [69] Thompson, A. P.; Aktulga, H. M.; Berger, R.; Bolintineanu, D. S.; Brown, W. M.; Crozier, P. S.; in't Veld, P. J.; Kohlmeyer, A.; Moore, S. G.; Nguyen, T. D., et al. LAMMPS—a flexible simulation tool for particle-based materials modeling at the atomic, meso, and continuum scales. *Computer Physics Communications* **2022**, *271*, 108171.
- [70] Martyna, G. J.; Klein, M. L.; Tuckerman, M. Nosé–Hoover chains: The canonical ensemble via continuous dynamics. *The Journal of chemical physics* **1992**, *97*, 2635–2643.
- [71] Martyna, G. J.; Tobias, D. J.; Klein, M. L. Constant pressure molecular dynamics algorithms. *The Journal of chemical physics* **1994**, *101*, 4177–4189.

- [72] Wen, M.; Shirodkar, S. N.; Plecháč, P.; Kaxiras, E.; Elliott, R. S.; Tadmor, E. B. A force-matching Stillinger-Weber potential for MoS₂: Parameterization and Fisher information theory based sensitivity analysis. *Journal of Applied Physics* **2017**, *122*, 244301.
- [73] Evans, D. J.; Holian, B. L. The nose–hoover thermostat. *The Journal of chemical physics* **1985**, *83*, 4069–4074.
- [74] Jena, N.; Ahammed, R.; Rawat, A.; Mohanta, M. K.; De Sarkar, A., et al. Valley drift and valley current modulation in strained monolayer MoS₂. *Physical Review B* **2019**, *100*, 165413.
- [75] Mohapatra, P.; Deb, S.; Singh, B.; Vasa, P.; Dhar, S. Strictly monolayer large continuous MoS₂ films on diverse substrates and their luminescence properties. *Applied Physics Letters* **2016**, *108*, 042101.
- [76] Qian, X.; Liu, J.; Fu, L.; Li, J. Quantum spin Hall effect in two-dimensional transition metal dichalcogenides. *Science* **2014**, *346*, 1344–1347.
- [77] Li, T. Ideal strength and phonon instability in single-layer MoS₂. *Physical Review B* **2012**, *85*, 235407.
- [78] Bera, J.; Sahu, S. Strain induced valley degeneracy: a route to the enhancement of thermoelectric properties of monolayer WS₂. *RSC advances* **2019**, *9*, 25216–25224.
- [79] Guo, S.-D. Biaxial strain tuned thermoelectric properties in monolayer PtSe₂. *Journal of Materials Chemistry C* **2016**, *4*, 9366–9374.
- [80] Cai, Y.; Lan, J.; Zhang, G.; Zhang, Y.-W. Lattice vibrational modes and phonon thermal conductivity of monolayer MoS₂. *Physical Review B* **2014**, *89*, 035438.
- [81] Mobaraki, A.; Kandemir, A.; Yapicioglu, H.; Gülseren, O.; Sevik, C. Validation of inter-atomic potential for WS₂ and WSe₂ crystals through assessment of thermal transport properties. *Computational Materials Science* **2018**, *144*, 92–98.
- [82] Sevik, C. Assessment on lattice thermal properties of two-dimensional honeycomb structures: Graphene, h-BN, h-MoS₂, and h-MoSe₂. *Physical Review B* **2014**, *89*, 035422.
- [83] Huang, L. F.; Gong, P. L.; Zeng, Z. Correlation between structure, phonon spectra, thermal expansion, and thermomechanics of single-layer MoS₂. *Physical Review B* **2014**, *90*, 045409.
- [84] Bardeen, J.; Shockley, W. Deformation potentials and mobilities in non-polar crystals. *Physical review* **1950**, *80*, 72.
- [85] Wiktor, J.; Pasquarello, A. Absolute deformation potentials of two-dimensional materials. *Physical Review B* **2016**, *94*, 245411.
- [86] Hung, N. T.; Nugraha, A. R.; Saito, R. Two-dimensional MoS₂ electromechanical actuators. *Journal of Physics D: Applied Physics* **2018**, *51*, 075306.
- [87] Laturia, A.; Van de Put, M. L.; Vandenberghe, W. G. Dielectric properties of hexagonal boron nitride and transition metal dichalcogenides: from monolayer to bulk. *npj 2D Materials and Applications* **2018**, *2*, 1–7.
- [88] Rawat, A.; Jena, N.; De Sarkar, A., et al. A comprehensive study on carrier mobility and artificial photosynthetic properties in group VI B transition metal dichalcogenide monolayers. *Journal of Materials Chemistry A* **2018**, *6*, 8693–8704.
- [89] Ding, Z.; Yang, S.-W.; Wu, G.; Yang, X. Geometry and Greatly Enhanced Thermoelectric Performance of Monolayer MXY Transition-Metal Dichalcogenide: MoSTe as an Example. *physica status solidi (RRL)–Rapid Research Letters* **2021**, *15*, 2100166.
- [90] Zhang, Y.; Ye, J.; Matsushashi, Y.; Iwasa, Y. Ambipolar MoS₂ thin flake transistors. *Nano letters* **2012**, *12*, 1136–1140.
- [91] Peng, J.; Najmaei, S.; Dubey, M.; Chung, P. W. Dominant ZA phonons and thermal carriers in HfS₂. *Journal of Applied Physics* **2019**, *126*, 164302.
- [92] Peng, B.; Zhang, H.; Shao, H.; Xu, Y.; Zhang, X.; Zhu, H. Thermal conductivity of monolayer MoS₂, MoSe₂, and WS₂: interplay of mass effect, interatomic bonding and anharmonicity. *RSC advances* **2016**, *6*, 5767–5773.
- [93] Slack, G. A. Nonmetallic crystals with high thermal conductivity. *Journal of Physics and Chemistry of Solids* **1973**, *34*, 321–335.